

RESEARCH

Open Access



# CPHNet: a novel pipeline for anti-HAPE drug screening via deep learning-based Cell Painting scoring

De-zhi Sun<sup>2†</sup> , Xi-ru Yang<sup>1,2†</sup>, Cong-shu Huang<sup>3†</sup>, Zhi-jie Bai<sup>2</sup>, Pan Shen<sup>2</sup>, Zhe-xin Ni<sup>2</sup>, Chao-ji Huang-fu<sup>2</sup>, Yang-yi Hu<sup>1</sup>, Ning-ning Wang<sup>2</sup>, Xiang-lin Tang<sup>2</sup>, Yong-fang Li<sup>1</sup>, Yue Gao<sup>1,2,4\*</sup>  and Wei Zhou<sup>1,2\*</sup> 

## Abstract

**Background** High altitude pulmonary edema (HAPE) poses a significant medical challenge to individuals ascending rapidly to high altitudes. Hypoxia-induced cellular morphological changes in the alveolar-capillary barrier such as mitochondrial structural alterations and cytoskeletal reorganization, play a crucial role in the pathogenesis of HAPE. These morphological changes are critical in understanding the cellular response to hypoxia and represent potential therapeutic targets. However, there is still a lack of effective and valid drug discovery strategies for anti-HAPE treatments based on these cellular morphological features. This study aims to develop a pipeline that focuses on morphological alterations in Cell Painting images to identify potential therapeutic agents for HAPE interventions.

**Methods** We generated over 100,000 full-field Cell Painting images of human alveolar adenocarcinoma basal epithelial cells (A549s) and human pulmonary microvascular endothelial cells (HPMECs) under different hypoxic conditions (1%–5% of oxygen content). These images were then submitted to our newly developed segmentation network (SegNet), which exhibited superior performance than traditional methods, to proceed to subcellular structure detection and segmentation. Subsequently, we created a hypoxia scoring network (HypoNet) using over 200,000 images of subcellular structures from A549s and HPMECs, demonstrating outstanding capacity in identifying cellular hypoxia status.

**Results** We proposed a deep neural network-based drug screening pipeline (CPHNet), which facilitated the identification of two promising natural products, ferulic acid (FA) and resveratrol (RES). Both compounds demonstrated satisfactory anti-HAPE effects in a 3D-alveolus chip model (ex vivo) and a mouse model (in vivo).

**Conclusion** This work provides a brand-new and effective pipeline for screening anti-HAPE agents by integrating artificial intelligence (AI) tools and Cell Painting, offering a novel perspective for AI-driven phenotypic drug discovery.

**Keywords** High altitude pulmonary edema (HAPE), Artificial intelligence (AI), Drug discovery, Cell painting

<sup>†</sup>De-zhi Sun, Xi-ru Yang and Cong-shu Huang contributed equally to this work.

\*Correspondence:

Yue Gao  
gaoyue@bmi.ac.cn  
Wei Zhou  
zhouweisy1802@163.com

<sup>1</sup>Department of Pharmacy, Medical College of Qinghai University, Xining, Qinghai 810001, China

<sup>2</sup>Department of Pharmaceutical Sciences, Beijing Institute of Radiation Medicine, No. 27, Taiping Road, Haidian District, Beijing 100850, China

<sup>3</sup>Traditional Chinese Medicine School, Henan University of Chinese Medicine, Zhengzhou, Henan 450046, China

<sup>4</sup>State Key Laboratory of Kidney Diseases, Chinese PLA General Hospital, Beijing 100853, China



© The Author(s) 2025. **Open Access** This article is licensed under a Creative Commons Attribution-NonCommercial-NoDerivatives 4.0 International License, which permits any non-commercial use, sharing, distribution and reproduction in any medium or format, as long as you give appropriate credit to the original author(s) and the source, provide a link to the Creative Commons licence, and indicate if you modified the licensed material. You do not have permission under this licence to share adapted material derived from this article or parts of it. The images or other third party material in this article are included in the article's Creative Commons licence, unless indicated otherwise in a credit line to the material. If material is not included in the article's Creative Commons licence and your intended use is not permitted by statutory regulation or exceeds the permitted use, you will need to obtain permission directly from the copyright holder. To view a copy of this licence, visit <http://creativecommons.org/licenses/by-nc-nd/4.0/>.

## Background

High altitude pulmonary edema (HAPE) presents a significant medical challenge, particularly to individuals rapidly ascending to high altitudes without adequate acclimatization [1, 2]. This condition, characterized by fluid accumulation in the lung, can rapidly progress to a life-threatening state if left unaddressed [3]. The onset of HAPE involves complex factors, including pulmonary hypertension, inflammation, and changes in the alveolar-capillary barrier. However, the specific mechanisms remain unclear [4, 5]. Recent studies indicate that hypoxia and pulmonary hypertension can lead to the activation of VEGF signaling, resulting in increased permeability of the alveolar-capillary barrier [6, 7]. This change is likely a key factor in HAPE pathogenesis, as it allows fluid to leak into the alveolar spaces, leading to pulmonary edema [1]. Additionally, hypoxia-induced morphological and functional alterations in the vascular endothelial cells and alveolar epithelial cells are considered critical determinants in the pathogenesis of pulmonary hypertension [8, 9]. Thus, it is worthwhile to develop models to investigate the interventional effects of agents on hypoxia-induced cellular changes in order to facilitate the efficient screening of potential anti-HAPE agents.

Cell Painting, an evolution of high content screening (HCS), employs six different dyes to stain various subcellular structures and images them across multiple channels [10]. This technology can identify the mechanism of action (MoA) of agents early in drug development, guiding hit expansion based on structure-phenotype relationships, and avoiding the misinterpretation associated with nominal targets [11, 12]. Cell Painting can provide comprehensive morphological data, enhance the reliability of phenotypic analyses and facilitate the rapid identification of agents that effectively improve HAPE-related cellular phenotypes, thus increasing success rates of screening and accelerating drug development [13]. Despite this, the unbiased quantitative evaluation of morphological changes in a large number of Cell Painting images is challenging using conventional methods. A scoring system that can quantitatively assess cellular states could be a crucial tool for drug screening, enabling more accurate and efficient identification of promising therapeutic agents [14, 15]. Recent advancements in deep learning have significantly enhanced the analysis of cellular images, offering efficient tools for interpreting complex morphological changes [16, 17]. These AI methods, such as the YOLO family [18], could effectively extract individual cells and identify intricate morphological features from high-content images, facilitating rapid and automated classification of cellular phenotypes as well as precise assessment of drug effects [19–21].

The actual physiological environment involves intricate interactions among multiple cell types within complex

three-dimensional structures, which conventional two-dimensional cell cultures cannot adequately replicate. Organ-on-chip (OoC) technology effectively bridges this gap by simulating key physiological conditions, such as cell-to-cell interactions and mechanical forces, offering a model that more closely resembles the *in vivo* human environment [22]. Compared to traditional cell culture methods, OoC technology provides a more accurate assessment of drug efficacy while significantly reducing the reliance on animal testing [23]. However, *in vivo* models remain indispensable for validating the accuracy and translational relevance of *in vitro* findings. C57BL/6 mice, for instance, exhibit hypoxia-induced inflammatory responses in lung tissues that closely mirror the mechanisms observed in human HAPE, making them particularly suitable for confirming the reliability of OoC data and ensuring that these microphysiological systems can effectively translate into clinical applications [24–26].

In this study, we hypothesized that deep learning could accurately identify morphological alterations of hypoxic cells from Cell Painting images and propose a novel pipeline, CPHNet, for the identification of potential therapeutics for HAPE (Fig. S1). This pipeline transitions the screening process from a manual or semi-automated procedure to a fully automated one by employing two deep learning models: a segmentation network (SegNet) and a Hypoxia Scoring Network (HypoNet). SegNet effectively detects and segments subcellular structures in full-field images of A549 and HPMECs. HypoNet excels at assessing the extent of hypoxia in these cells. Finally, we applied CPHNet in screening potential anti-HAPE agents and validated the results using OoC technology and animal models.

## Methods

### Cell culture and hypoxia treatment

#### Training group

In accordance with the manufacturer's instructions, A549 and HPMEC cell lines (obtained from the ATCC cell repository) were cultured in DMEM with the addition of 10% FBS, L-glutamine (0.292 mg/ml), penicillin (100 U/ml), and streptomycin (100 mg/ml). The cells were seeded at a density of 8000 cells per well in PhenoPlate™-Ultra 96-well black plates (PerkinElmer, 6055302). Four parallel plates were prepared for each cell line and were incubated overnight in a 37 °C, 5% CO<sub>2</sub> cell culture incubator. Post-adherence, three of the plates for every cell line were transferred to hypoxic culture chambers set at oxygen levels of 1%, 3%, and 5% respectively, with the conditions maintained at 37 °C and 5% CO<sub>2</sub> for a duration of 24 h. Meanwhile, the fourth plate for each cell line was left cultured under standard oxygen concentration during the same timeframe. Subsequently, the four plates underwent cell staining and imaging.

### Screening group

A549 and HPMEC were divided into one normoxia group (NH), one 5% hypoxia group (HY), and eleven hypoxia treatment groups, totaling 13 groups ( $n=6$ ). Each group was seeded with 3000 cells per well in black plates. After cell adhesion, the hypoxia treatment groups underwent medium changes, and 0.1  $\mu\text{M}$  tetramethylpyrazine (Macklin, T819555), 0.68  $\mu\text{M}$  tanshinone IIA (MCE, HY-N0135), 0.64  $\mu\text{M}$  salvianolic acid B (MCE, HY-N1362), 0.05  $\mu\text{M}$  salvianolic acid C (MCE, HY-N0319), 0.05  $\mu\text{M}$  20(S)-ginsenoside Rh2 (Chinese Pharmacopoeia Institute, 111748), 0.05  $\mu\text{M}$  acetazolamide (Aladdin, A194116), 0.1  $\mu\text{M}$  catechin (MCE, HY-N0898), 0.1  $\mu\text{M}$  resveratrol (Chinese Pharmacopoeia Institute, 111535), 0.025  $\mu\text{M}$  ferulic acid (Chinese Pharmacopoeia Institute, 110773), 0.01  $\mu\text{g/ml}$  compound Danshen dripping pills (National Medical Products Administration, Z10950111), and 0.005  $\mu\text{g/ml}$  Hongyi capsules (Military Medicine Approval, Z2019006) were added in a medium change format (Fig. S2). The NH group and HY group underwent regular medium changes. After 24 h of incubation, the HY group and hypoxia treatment groups were transferred to a three-gas hypoxic culture chamber for an additional 24 h, with the NH group cultured under normal oxygen concentration during this period. Following removal, the cells were stained and imaged.

### Cell staining

PhenoVue Cell Imaging Kit contains six dyes necessary for cell imaging experiments. These dyes corresponded to various cellular compartments: the 33,342 Nuclear Stain marked DNA; the 488 Concanavalin A marked the endoplasmic reticulum; the 512 Nuclear Acid Stain marked nucleoli and cytoplasmic RNA; the 568 Phalloidin were used to label the actin cytoskeleton; the 555 WGA marked plasma membrane and Golgi apparatus; and the 641 Mitochondrial Stain marked mitochondria. We substituted PhenoVue Fluor 555-WGA with CellBrite Fix 555 (Biotium, 30088 A). PhenoVue Fluor 641-Mitochondrial Stain and PhenoVue Fluor 512-Nucleic Acid Stain were combined in a dye dilution solution to prepare Staining Solution 1, while the remaining dyes were diluted in another solution to prepare Staining Solution 2.

After removal of the culture medium, 50  $\mu\text{l}$  of Staining Solution 1 was added to each well and incubated in the dark at 37  $^{\circ}\text{C}$ , 5%  $\text{CO}_2$  for 30 min. The cells were washed three times with 100  $\mu\text{l}$  of HBSS solution (Gibco, 2507502) per well. Then, 15  $\mu\text{l}$  of 16% PFA was added to each well and the cells were fixed at room temperature for 20 min, followed by one wash with HBSS solution. Subsequently, 50  $\mu\text{l}$  of 0.1% Triton X-100 solution was added to each well and incubated at room temperature in

the dark for 15 min to increase cell permeability. The cells were washed twice with HBSS solution.

Afterwards, 50  $\mu\text{l}$  of Staining Solution 2 was added to each well and incubated in the dark at room temperature for 30 min. The cells were washed three times with 100  $\mu\text{l}$  of HBSS solution, with the final HBSS solution being retained. The samples were stored in the dark.

### Multi-channel cellular imaging

The microplate was placed in the Opera Phoenix high-content imaging system, and the microscope acquisition settings were configured following the description by Bray et al. [10]. Cells were imaged at 60 $\times$  magnification using a water-immersion objective. To ensure unbiased results, multiple full-field images were captured per well using six different wavelength ranges according to the application note (Table S1). The exported grayscale images were processed using ImageJ, which transformed the original images into RGB pseudo-colored versions, thereby improving the extraction of features from different cellular compartments.

### Data preprocessing for SegNet

To achieve deep learning-based segmentation and extraction of individual cells, we built our segmentation network (SegNet) using transfer learning based on the YOLO v8n framework. The source dataset comprised thousands of grayscale images from six subcellular structures, namely nucleus (DNA), endoplasmic reticulum (ER), actin/Golgi apparatus (AG), mitochondria (Mito), plasma membrane (PM) and RNA. For the convenience of visual observation and manual annotation, we developed an ImageJ plugin to convert these grayscale images into pseudo-color images. Subsequently, we constructed two training datasets through manual annotation, one for cell nucleus segmentation (NS) and the other for cell membrane segmentation (MS). Manual annotation refers to the use of specialized annotation software, named LabelMe (version 5.2.1), to manually outline masks that cover the regions of cell nucleus or membranes in a full-field image by selecting vertices to generate polygons. It's important to highlight that prior to manual annotation, we merged the original grayscale images of DNA, AG, and PM into a single DAP RGB pseudo-colored image, thereby creating the MS dataset. The reason for including the DNA in the MS images was that the presence of the nucleus could make it easier to identify the cell's location, and it can provide guidance for membrane localization.

### Training of SegNet

SegNet was designed to simultaneously perform NS and MS tasks. For NS, the segmentation object was DNA, while for MS, the segmentation object was DAP.

To train the model, we input our NS and MS set together. We customized the hyperparameters of the model, including the number of training epochs (200), image size (960 pixels), number of workers [8], batch size [8], initial learning rate (0.01), and learning rate decay factor (0.01). Furthermore, we utilized transfer learning in the training process by incorporating pre-trained weights. During our training process, we employed various data augmentation techniques to enhance the diversity and robustness of our dataset, such as translation, scaling, horizontal flipping, and mosaic augmentation.

### Evaluation of SegNet

Mean Average Precision (mAP) is a commonly employed metric to assess the effectiveness of object detection and segmentation algorithms. mAP@0.5 calculates the Average Precision (AP) for each class when the Intersection over Union (IoU) threshold is set to 0.5. The mAP is then obtained by averaging the AP values across all classes. mAP@0.5:0.95 represents the mAP across various IoU thresholds, ranging from 0.5 to 0.95 with a step size of 0.05.

$$\text{IoU} = \frac{\text{TP}}{\text{FP} + \text{TP} + \text{FN}} \quad (1)$$

In addition, to compare with the segmentation performance of CellProfiler (CP) [10] and Mask R-CNN, we prepared an independently labeled test set, ensuring that each view included both DNA and DAP images. After generating corresponding masks, we compared the recall, precision, F1-score and processing speed among the three methods.

### Cell segmentation and subcellular structure extraction

We processed the full-field images of DNA and DAP using the pre-trained SegNet to predict object boundaries of nuclear and membrane structures. For each object, the coordinates of the boundary points were extracted to create binary masks with regions with a pixel value of 1 representing the object boundaries and regions with a pixel value of 0 representing the background. To assess the correspondence between masks and objects, we introduced a custom nucleus-membrane matching algorithm (NMM, Table S2) that determined whether the masks of two objects corresponded to the nucleus and membrane from the same cell. The masks' match was determined by finding out whether the boundary points of one mask were contained within the other while avoiding edge areas of the image. Through this process, we obtained the spatial coordinates of the nuclei and cell membranes of individual cells in the field of view for the extraction of subcellular structures.

Once a match was identified, individual subcellular structure images were created by copying pixel values from the original images according to the masks. Images for DNA, AG, ER, Mito, PM and RNA structures were created accordingly. The detailed operations for each channel were as follows:

$$\begin{aligned} I_j^D &= I^D \times M_j^D \\ I_j^E &= I^E \times (M_k^A - M_j^D) \\ I_j^A &= I^A \times M_k^A \\ I_j^M &= I^M \times (M_k^A - M_j^D) \\ I_j^P &= I^P \times M_k^A \\ I_j^R &= I^R \times M_k^A \end{aligned} \quad (2)$$

The variables  $j$  and  $k$  represent the indices of matched cell nucleus and membranes, respectively. The variables  $I$  and  $M$  correspond to the image and mask matrix of each subcellular structure, with superscripts  $D$ ,  $E$ ,  $A$ ,  $M$ ,  $P$  and  $R$  representing the DNA, ER, AG, Mito, PM and RNA channels, respectively.

### Analysis of morphological features in cell painting images

To extract morphological features of each subcellular structure and optical characteristics of the images, we developed a workflow based on the Scikit-Image library (version 0.21.0). Using the DNA mask, such features as the nucleus area, perimeter, shape factor, aspect ratio, and contour were computed. Using the DAP mask, features like the cell area, perimeter, shape factor, aspect ratio, and contour were calculated in a similar manner. For each of the subcellular structures (DNA, AG, ER, Mito, RNA, PM), GLCM properties (contrast, dissimilarity, homogeneity, energy, correlation, ASM) were computed for texture analysis. Additional features including granularity and mean intensity were also measured.

Furthermore, we generated a clustered heatmap of the normalized data using Seaborn library (version 0.12.2), clustering the columns to highlight the correlations between different features. We adopted t-Distributed Stochastic Neighbor Embedding (t-SNE) to visualize the features and to observe the similarity among cells within and between different groups.

### Customized ResNet-50-based hypoxia scoring network (HypoNet)

In this work, we presented a customized HypoNet based on ResNet-50, which classified cells as experiencing hypoxia or being in a normoxic state. While ResNet-50 is traditionally designed for three-channel input (RGB images), we made a noteworthy adaptation by extending it to process input data with six channels (DNA, AG, ER, Mito, PM and RNA). As our research focused on a binary

classification problem, the output layer was modified to 2 dimensions, in which the activation function used was the sigmoid function. We implemented HypoNet using PyTorch (version 1.13.1).

### Training of HypoNet

First, we resized the six-channel individual subcellular structure images as mentioned above to  $224 \times 224$  pixels using the OpenCV library. Additionally, we created training (80%) and validation (20%) datasets through a random split. The binary cross-entropy loss function (BCELoss) was selected as the optimization objective. We employed stochastic gradient descent (SGD) as the optimization algorithm with a momentum of 0.9 and a weight decay of 0.0005.

We normalized input images using the following transformation:

$$Y = \left( \frac{X}{255} - 0.5 \right) \times 2 \quad (3)$$

$Y$ : the values of normalized images, and  $X$ : the values of the original images.

The model underwent 20 epochs of training with an initial learning rate of 0.01. The first epoch used a smaller learning rate as a warm-up before switching to the initial learning rate. The learning rate was reduced by a factor of 0.2 at predefined milestones (6, 12, and 18 epochs). All training was performed on an environment equipped with two NVIDIA GeForce RTX 3090 GPUs.

### Evaluation metrics for HypoNet

The performance of HypoNet was assessed using several metrics, including accuracy, precision, recall, F1-score, and the Area Under the Curve (AUC).

$$\begin{aligned} \text{accuracy} &= \frac{\text{TP} + \text{TN}}{\text{TP} + \text{FP} + \text{TN} + \text{FN}} \\ \text{precision} &= \frac{\text{TP}}{\text{TP} + \text{FP}} \\ \text{recall} &= \frac{\text{TP}}{\text{TP} + \text{FN}} \\ \text{F1-score} &= 2 \times \frac{\text{Recall} \times \text{Precision}}{\text{Recall} + \text{Precision}} \end{aligned} \quad (4)$$

To validate the superiority of our neural network architecture, we conducted a comparative analysis on an independent test set against four distinct neural network structures employed in hypoxia classification models: VGG-16, GoogleNet, Xception, and Deep-SeaMo [17]. Each network underwent similar modifications and training processes using the same dataset and training parameters as those used for HypoNet. Post-training, we assessed the models' performance on the test set,

focusing on metrics mentioned above, to evaluate their generalization capabilities.

To visualize the features detected by HypoNet, we extracted parameters from the top convolutional layer and flattened them into a 2048-dimensional array. Subsequently, t-SNE was employed to cluster these outputs.

### Hypoxia scoring for individual cells by HypoNet

The hypoxia score was calculated based on the probability of hypoxia, indicating each cell's likelihood of being hypoxic as determined by the outputs of the pre-trained HypoNet, at the single-cell resolution. The neural network calculated the probability class of input data using the sigmoid function in the output layer:

$$\text{sigmoid: } y_i = \frac{1}{1 + e^{-x_i}} \quad (5)$$

The average hypoxia score was determined by averaging the probabilities of belonging to the hypoxia class across all input datasets:

$$\text{hypoxia score} = \frac{\sum_{k=1}^m P_k^H}{m} \quad (6)$$

Where  $m$  is the number of input datasets, and  $P_k^H$  is the probability of belonging to the hypoxia class in each input dataset.

### 3D-alveolus chip model

#### Chip Preparation

The chips and microfluidic devices (Synvivo Ltd, CAT#405001) were designed with a polydimethylsiloxane (PDMS) porous membrane, creating two or more parallel cavities. Collagen type IV (Sigma, C5533-5MG) was infused into the cavities to promote cell attachment along the periphery, while the central region permitted gas or liquid flow. Capillaries within the porous membranes facilitated the transport of sub-10  $\mu\text{m}$  materials, enabling cell-cell interactions and nutrient exchange, thereby closely replicating the alveolar-capillary barrier.

#### Cell culture

A549s ( $5 \sim 10 \times 10^6$  cells/ml) were seeded into the channels of a collagen-coated chip and placed vertically. After the cells adhered to the walls, the chip was inverted, and HPMECs ( $1 \sim 5 \times 10^6$  cells/ml) were seeded into the lower channel. Once attached, a constant flow of medium ( $0.1 \sim 1 \mu\text{l}/\text{min}$ ) was applied to both upper and lower channels. Co-culture was carried out for 3 to 7 days, with medium change at  $3 \mu\text{l}/\text{min}$  daily. Once a confluent monolayer of both cell types was formed, drug-containing medium was introduced to the treatment group chips and circulated for 24 h. Gas was slowly introduced into

the upper channel, and a mixture of alveolar epithelial and endothelial cell media (1:1) was introduced into the lower channel and incubated for 24 h at 37 °C.

#### **Permeability assessment**

The permeability of the alveolar-capillary barrier was evaluated by measuring the diffusion rate of FITC-Dextran from the lower vascular layer to the upper alveolar channel [27]. After co-culture completion, channels were carefully rinsed with serum-free medium at a rate of 0.1 µl/min, followed by the introduction of serum-free medium containing FITC-Dextran solution (Sigma Aldrich 46944, 4 kDa, 0.05 mg/mL) at 0.5 µl/min into the lower channel of the chip. Fluorescence microscopy (Leica, DMI8 C 5400) was used to observe the center of the chip. Once the lower channel was filled with dye, the flow was stopped, tubes were clamped, and the chip was placed in an incubator. After 2 h of static culture, fluorescence images were captured (Ex/Em 485/520 nm), and the fluorescence intensities of the upper and lower channels were calculated using ImageJ.

#### **Immunofluorescence staining**

Channels were rinsed with 1× PBS to remove FITC solution, injected with 4% PFA and placed at room temperature for 15 min to fix cells, followed by incubation with immunofluorescence blocking solution (beyotime, P0102) for 3 h at room temperature. Antibodies were diluted in 1% BSA and incubated with corresponding primary antibodies overnight at 4 °C, followed by secondary antibodies for 1 h at room temperature. After staining with secondary antibodies, cell nuclei were counterstained with 4',6-diamidino-2-phenylindole (DAPI). Confocal imaging was performed (Zeiss LSM980), and images were processed using Zeiss Zen 3.8 software.

#### **Cytokine analysis**

Cells from both the alveolar and vascular channels of each chip were digested, lysed on ice, and the supernatant was collected. Concentration of Vascular Endothelial Growth Factor (VEGF) was measured using respective human ELISA kits (JINGMEI BIOTECHNOLOGY, China) according to the manufacturer's instructions. Measured concentration (pg/ml) was converted to fold changes relative to the NH group.

#### **Source of animals**

Male C57BL/6J mice (8 weeks old, approximately 22 g) were purchased from Jiangsu Jicui Yaokang Biotechnology Co., Ltd. All mice were bred under standard conditions.

#### **The LPS-induced hypoxia experiment**

Mice were randomly divided into four groups: Normoxia group (NH,  $n=16$ ), Hypoxia group (HY,  $n=16$ ), Hypoxia+FA group (FA,  $n=16$ ), and Hypoxia+RES group (RES,  $n=16$ ), with a total of 64 mice. For modeling, half an hour before hypoxia, 3 mg/kg of LPS was intraperitoneally injected, followed by placement in a hyperbaric oxygen chamber simulating an altitude of 7000 m for 24 h. Drug administration involved daily intraperitoneal injections of the respective drugs for one week prior to hypoxia; the NH and HY groups received an equivalent volume of saline. The concentrations of the administered drugs were RES at 30 mg/kg (Aladin, R107315) and FA at 100 mg/kg (Merck, F809521).

#### **Detection of inflammatory factors in Bronchoalveolar lavage fluid (BALF)**

A midline incision was made along the trachea of the mouse, and 1 mL of pre-cooled PBS was slowly introduced into the trachea, allowed to stay for 2–3 s, and withdrawn. This process was repeated three times. The collected BALF was centrifuged at 5000 rpm for 10 min at 4 °C, and the supernatant was harvested and stored at -80 °C until further use. The concentrations of TNF-α (Jingmei, JM-02415M2), IL-6 (Jingmei, JM-02446M2), and VEGF (Perlay, AZ0626) in the supernatant were measured using ELISA kits according to the manufacturer's instructions.

#### **Pulmonary permeability**

One hour before the end of the scheduled hypoxia exposure, mice were injected with 200 µL of 2% Evan's Blue dye (YuanYe Bio, S19046) via the tail vein and continued to be exposed to hypoxia. After the hypoxia exposure, mice were euthanized by cervical dislocation, and 40 mL of saline was perfused through the right lobe of the heart to remove the dye from the blood vessels. The entire lung tissue was then excised, weighed, and rinsed in ice-cold saline. The tissue was divided into two parts: one was wrapped in foil and dried, and the other was homogenized in 10% PBS. The homogenate was incubated with three times the volume of formamide (SCR, 81007718) at 60 °C for 24 h, then centrifuged at 6000× for 15 min at 4 °C, or at 12,000 rpm for 10 min. The supernatant was collected, and the absorbance was measured at 620 nm using a microplate reader. Permeability results were expressed as the value of absorbance ( $OD_{620}$ ) per gram of dry weight.

#### **Western blot analysis**

Fifty milligrams of lung tissue were homogenized, and each sample was lysed with 220 µL of lysis buffer. The supernatant was collected and denatured, and protein was quantified by a Bicinchoninic acid kit. The proteins

were separated by electrophoresis and transferred onto a PVDF membrane (Millipore, IPVH00010). The membrane was incubated overnight at 4 °C with primary antibodies against IL-6, TNF- $\alpha$ , VEGF-A, and GAPDH (all at a 1:1000 dilution). After being washed with TBST buffer (LABLEAD, T7209B), the membrane was incubated with the corresponding secondary antibody (1:5000 dilution) at room temperature for 120 min. After another wash with TBST buffer, ECL detection was performed. The images were scanned, and grayscale analysis was conducted using ImageJ software, with GAPDH as the internal control for quantitative analysis. All primary antibodies are listed in Table S3.

### Hematoxylin and Eosin (H&E) staining

After the tissues were removed from formalin solution, they were embedded in paraffin. The tissues were stained using H&E staining and evaluated under a light microscope. The severity of pathological responses in the lungs included alveolar congestion, hemorrhage, neutrophil aggregation or leukocyte infiltration, and thickness of the alveolar wall.

### Statistical analysis

Statistical analysis was performed using SciPy (version 1.10.1) and Graphpad Prism (version 9.0.0). When conducting differential analysis of morphological features for each group, the Kruskal-Wallis test was applied. Dunnett's correction was employed for multiple testing, considering features with corrected p-values below 0.05 as significantly different. When comparing the average values among multiple groups, the standard deviation (SD) was used as a measure of intra-group variation.

## Results

### Dual segmentation of nuclear and membrane structures using SegNet

We acquired a total of 101,706 full-field cell images through the processes of drug administration, hypoxia culture, staining, and imaging. Each field of view contained six channels: DNA, ER, AG, Mito, PM, and RNA. To train the SegNet for individual cell detection and segmentation, we engaged three experts to manually annotate two datasets. The NS set consisted of 500 full-field DNA images for nucleus segmentation, while the MS set contained 500 full-field DAP images for membrane segmentation (Fig. 1A). These images were part of the Training Group collection. Both datasets contain approximately equaled quantities of A549 and HPMEC images. From these two datasets, 100 images from 50 views were randomly selected as the test set, while the remaining data were input into the SegNet for training. The training set comprises a total of over 18,000 DAP objects and 10,000 DNA objects (Fig. 1B).

During training, we employed data augmentation techniques such as scaling, rotation, and cropping of images (Fig. 1C). In the initial batches, our model demonstrated effective detection and segmentation of partial objects (Fig. 1D). As training progressed, the model's metrics exhibited perfect convergence. On the validation set, the model achieved a precision of 0.971, recall of 0.977, mAP@0.5 of 0.990, and mAP@0.5:0.95 of 0.938 (Fig. 1E). The F1-confidence curve of segmentation task was highly smooth, achieving its highest point at a confidence level of 0.4 with a peak value of 0.97, suggesting that the model demonstrated remarkable stability (Fig. 2A). The confusion matrix showed that out of 1856 DAP objects in the validation set, 1822 were correctly identified, and out of 1376 DNA objects, 1356 were correctly recognized. Moreover, there were no instances of confusion between DNA and DAP, indicating that SegNet was capable of precisely identifying and classifying the majority of objects (Fig. 2B). These results demonstrated that SegNet could accurately detect, classify, and segment both nuclei and cell membranes from full-field Cell Painting images.

### Comparison of image segmentation performance: AI vs. CellProfiler

To compare the effectiveness of SegNet, manual segmentation, and traditional segmentation methods such as CellProfiler (CP), we applied each method to segment the same image in the test set. The results indicated that our SegNet and manual segmentation performed similarly in terms of precision. Both achieved better segmentation of cell nuclei and membranes than CP (Fig. 2C). Due to the limitations of its principles, CP may incorrectly identify some pixels that do not belong to cell objects as part of cells. When cells were closely connected, SegNet exhibited superior segmentation performance compared to CP (Fig. 2D). Taking manual segmentation results as the ground truth, we compared various metrics (including recall, precision, F1-score) for the task of NS and MS (i.e., classifying pixels) by AI and CP on the test set. It was observed that except for DNA recall, our model's performance in NS and MS was superior to CP (Fig. 2E). CP's advantage in DNA recall mainly stems from its threshold segmentation strategy, leading to a decrease in precision, i.e., a high number of false-positive results. In terms of processing speed, our model demonstrated an impressive performance in that each image was analyzed in an average of only 22.2 milliseconds, compared with 110 milliseconds by Mask R-CNN, 1327 milliseconds by CP, and about 20 min by manual segmentation (Fig. S3).

### Morphological analysis of subcellular structures in hypoxia based on NMM

To extract the subcellular structure images, we first identified the object boundaries of nuclear and membrane

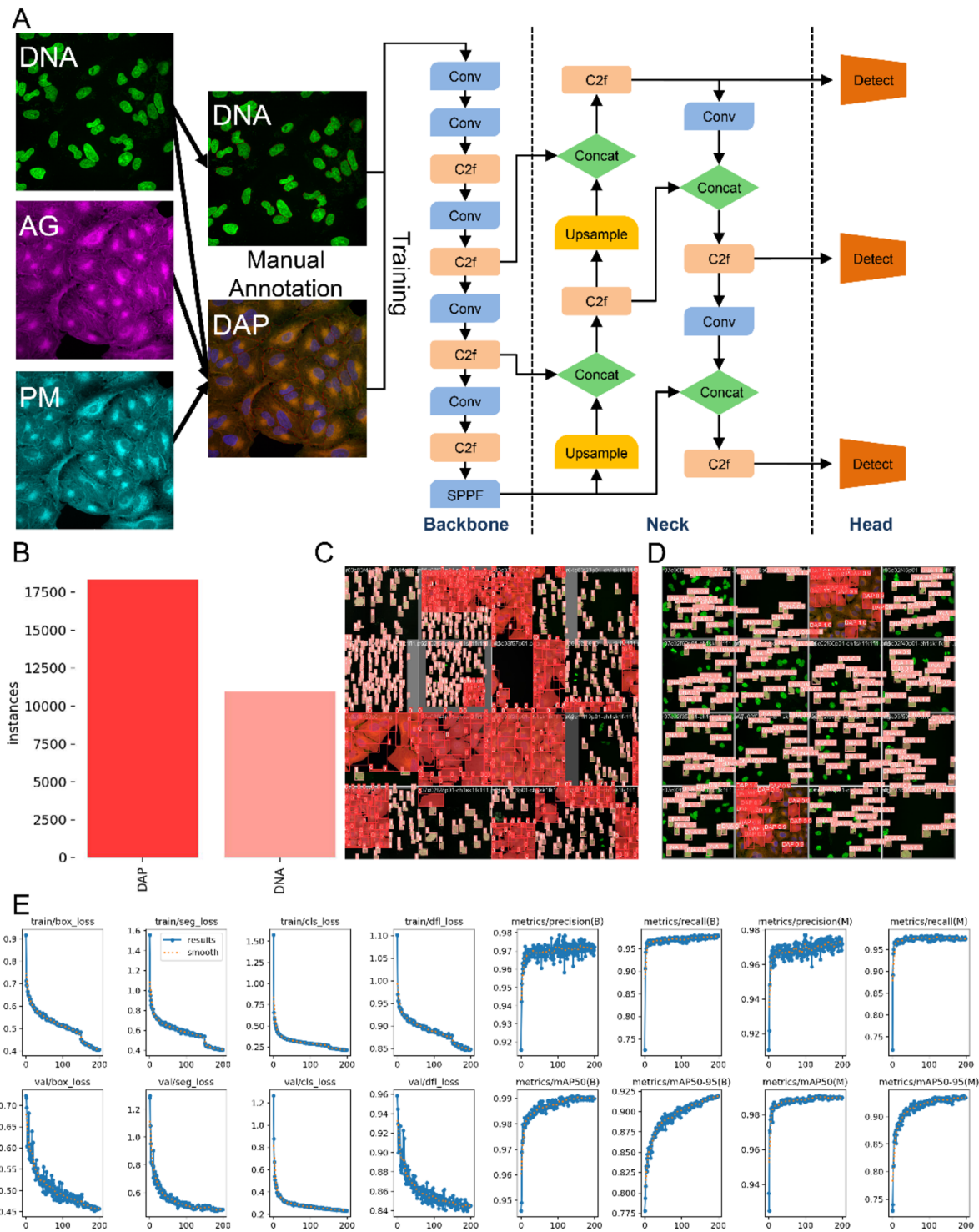


**Fig. 1** Comprehensive overview and performance of SegNet. **A.** Schematic diagram of the input and neural network structure of the SegNet. The input comprises two types of full-field images: DNA and DAP (integration of DNA, AG, and PM images). The red polygons in the images represent the manually annotated object boundaries. **B.** Histogram showing the total number of DAP and DNA objects contained in the training data, with the depth of color indicating the quantity. **C.** Display of training images after data augmentation processing. The masks and numbers indicate the masks of manually annotated object regions and their categories (0 for DAP, 1 for DNA), and the box is the smallest object boundary box automatically calculated from the mask. **D.** Initial phase of training, showing the model's object recognition and segmentation effects. The mask, box, letters, and numbers represent the mask of the object area recognized by the model, the boundary box, the object category label, and the probability, respectively. **E.** Training and validation performance of SegNet. Solid lines represent the real data trend, while dashed lines represent the trend after smoothing

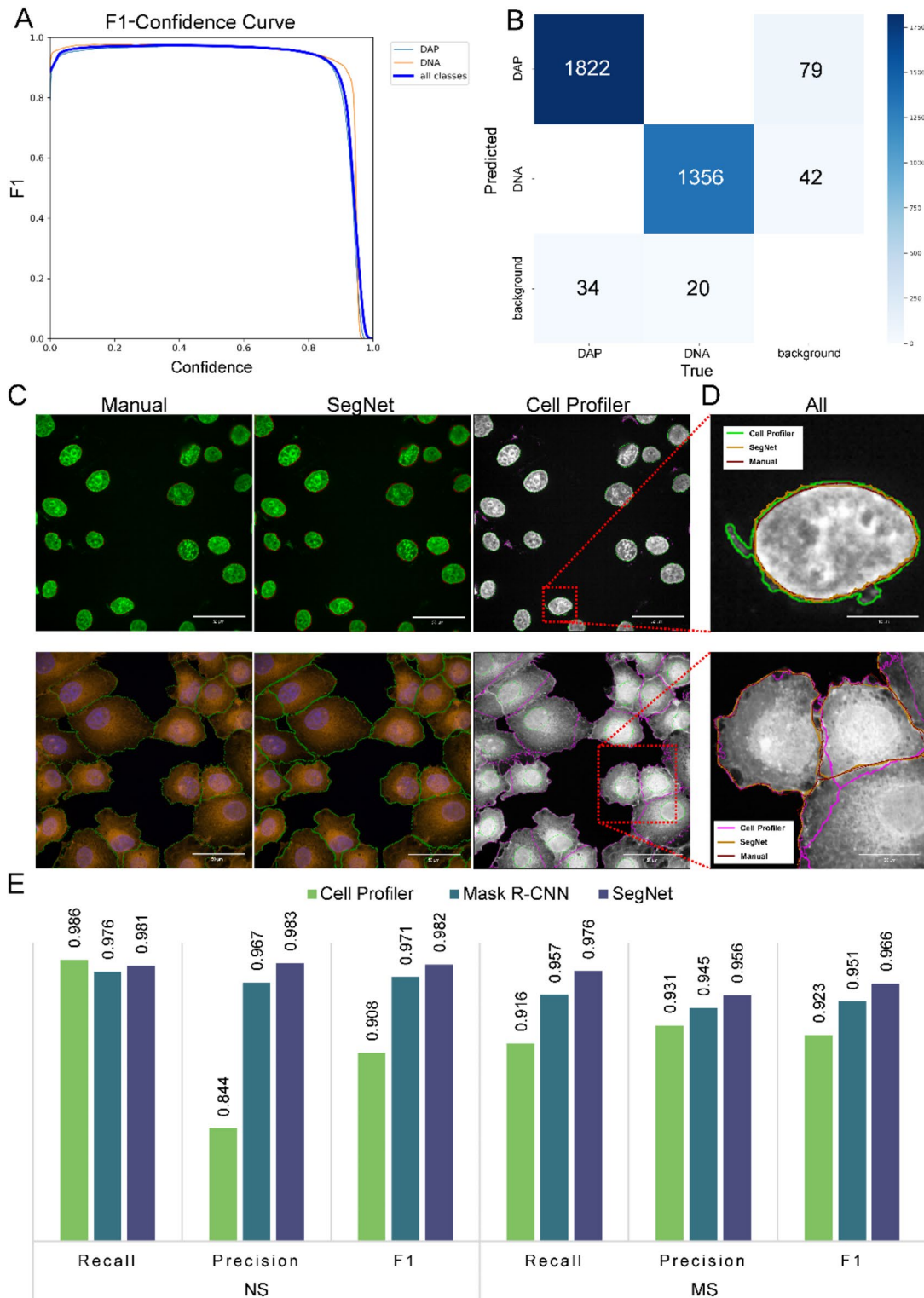


**Fig. 2** Evaluation of the cell segmentation models. **A** F1-Confidence curve of SegNet on the validation set. The curve depicts the F1-scores of the model across various confidence thresholds for identifying different objects, demonstrating the balance between precision and recall. **B** Confusion matrix of the SegNet on the validation set. Rows represent the categories predicted by the model, while columns represent the actual categories. Each cell's value indicates the number of samples for the corresponding combination of predicted and actual categories. Values on the main diagonal show the correct predictions for each category, while off-diagonal values indicate incorrect predictions. **C** The segmentation results obtained through manual, AI, and CP methods respectively. **D** A detailed comparative visualization of these three segmentation methods. The top row showcases the results of NS, and the bottom row features the outcomes of MS. **E** Evaluation of the three segmentation methods at the pixel level for NS and MS tasks on the test set

structures for single cells from full-field DNA and DAP images by employing our proposed nucleus-membrane matching algorithm (NMM). Subsequently, we generated individual subcellular structure images from full-field images based on the respective masks (Eq. 2), including DNA, AG, ER, Mito, PM, and RNA channels (Fig. 3A).

We then produced a new set of A549 Cell Painting data to verify our proposed method. This set included 846 full-field cell images under four oxygen concentration conditions (NH, 5% O<sub>2</sub>, 3% O<sub>2</sub>, and 1% O<sub>2</sub>). Using NMM, we obtained 56 morphological features of 6535 cells. The heatmap analysis indicated a high consistency in the measurement patterns of similar metrics. Furthermore, a number of these metrics showed variations that closely aligned with the gradient shifts in oxygen concentration among different groups (Fig. 3B). Volcano plot analysis indicated that compared to the NH group, the 5% O<sub>2</sub> group exhibited the most significant changes in mitochondrial morphology (Fig. 3D, S4A), while the 3% O<sub>2</sub> group showed significant changes in mitochondria, RNA, and cell membrane (Fig. 3E). Moreover, all morphological features in the 1% O<sub>2</sub> group underwent significant changes (Fig. S4B). However, a significant degree of variability was observed among cells within individual groups (Fig. 3B). The t-SNE visualization of these features highlighted a progressive alteration in the morphological characteristics of the cell population correlated with the decreasing levels of oxygen concentration (Fig. 3C). These findings vividly illustrated the impact of oxygen concentration on the morphological features of cells, indicating the practicality of performing drug screening grounded on changes in cellular phenotypes.

#### **HypoNet: evaluating and decoding cellular responses to hypoxia**

We trained HypoNet, designed for hypoxic cell classification, using a training dataset that included 150,696 images of subcellular structures from 8,830 A549s and 16,286 HPMECs as the negative set, along with 87,390 images from 6,011 A549s and 8,554 HPMECs under 1% oxygen conditions as the positive set from the Training Group (Fig. 4A). The model reached convergence around the 16th epoch, with accuracy, precision, recall, F1-score, and AUC all exceeding 0.97 on the validation set (Fig. 4B, S5). The output of the trained HypoNet was a non-linear prediction with two values, indicating either normoxic (0) or hypoxic [1].

To evaluate the generalization capability of our HypoNet, we conducted performance assessments on two independent test sets. The first comprised 2930 normoxic (NH) A549s and 4802 A549s treated with 1% O<sub>2</sub>. The second set included 2809 NH HPMECs and 3813 HPMECs also treated with 1% O<sub>2</sub>. These data sets were entirely independent of the training set. Additionally,

we compared the model's performance with that of four other state-of-the-art (SOTA) neural network architectures. The results indicated that our HypoNet model outperformed the other four SOTA neural network architectures (VGG-16, GoogleNet, Xception, and DeepSeSMo) on A549s, achieving an accuracy of 84.7%, recall of 81.9%, precision of 96.7%, F1-score of 88.7%, and an AUC of 0.808. In HPMECs, HypoNet showed even more remarkable performance, with an accuracy of 88.9%, recall of 87.4%, precision of 96.7%, F1-score of 91.8%, and an AUC of 0.856. In contrast, other models demonstrated significantly lower performance on HPMECs, especially the DeepSeSMo model, which showed the lowest accuracy of 42.9% and an F1-score of 33.7% (Table 1).

To investigate the cellular response to hypoxia and the relationship with the intensity of hypoxic stress induction, we input subcellular structure images of the four groups of A549s mentioned in the previous section into HypoNet, and visualized parameters of the top convolutional layer using t-SNE (Fig. 4C). The results showed that the distribution of top layer parameters exhibited a more pronounced trend than morphological features (Fig. S7). This suggested that our HypoNet was more sensitive in capturing the morphological alterations in cells induced by hypoxia. Furthermore, it indicated that the cellular response to hypoxic conditions could be quantitatively measured in a way that corresponded with the intensity of the stress. We then employed HypoNet to conduct hypoxia scoring on the identical dataset. In an interesting observation, the hypoxia scores were almost binary at the single-cell level in the training set, either around 0 or 1. Yet, a more nuanced picture emerged when comparing the average scores across the four groups: they reflect the gradation in hypoxia induction strength (Fig. 4D).

Subsequently, we conducted a second investigation of the cellular morphological alterations under various hypoxic conditions and proceeded to assess the interpretability of the HypoNet. The observations revealed significant morphological transformations in the mitochondria of cells with high hypoxia scores, shifting from elongated filamentous structures to more rounded and fragmented forms, with a tendency to cluster around the cell nucleus. Additionally, signals of dispersed vesicular structures were observed as dispersed bright spots in channels such as PM, likely indicating the activation of autophagy as an adaptive survival mechanism in response to hypoxic stress (Fig. 4E) [28]. Our model effectively identified such signals in cells with higher hypoxia scores, while they were rarely present in cells with very low hypoxia scores (Fig. S8). These findings not only revealed a close correlation between hypoxia scores and cellular morphological responses but also suggested the potential applicability of HypoNet in drug screening.

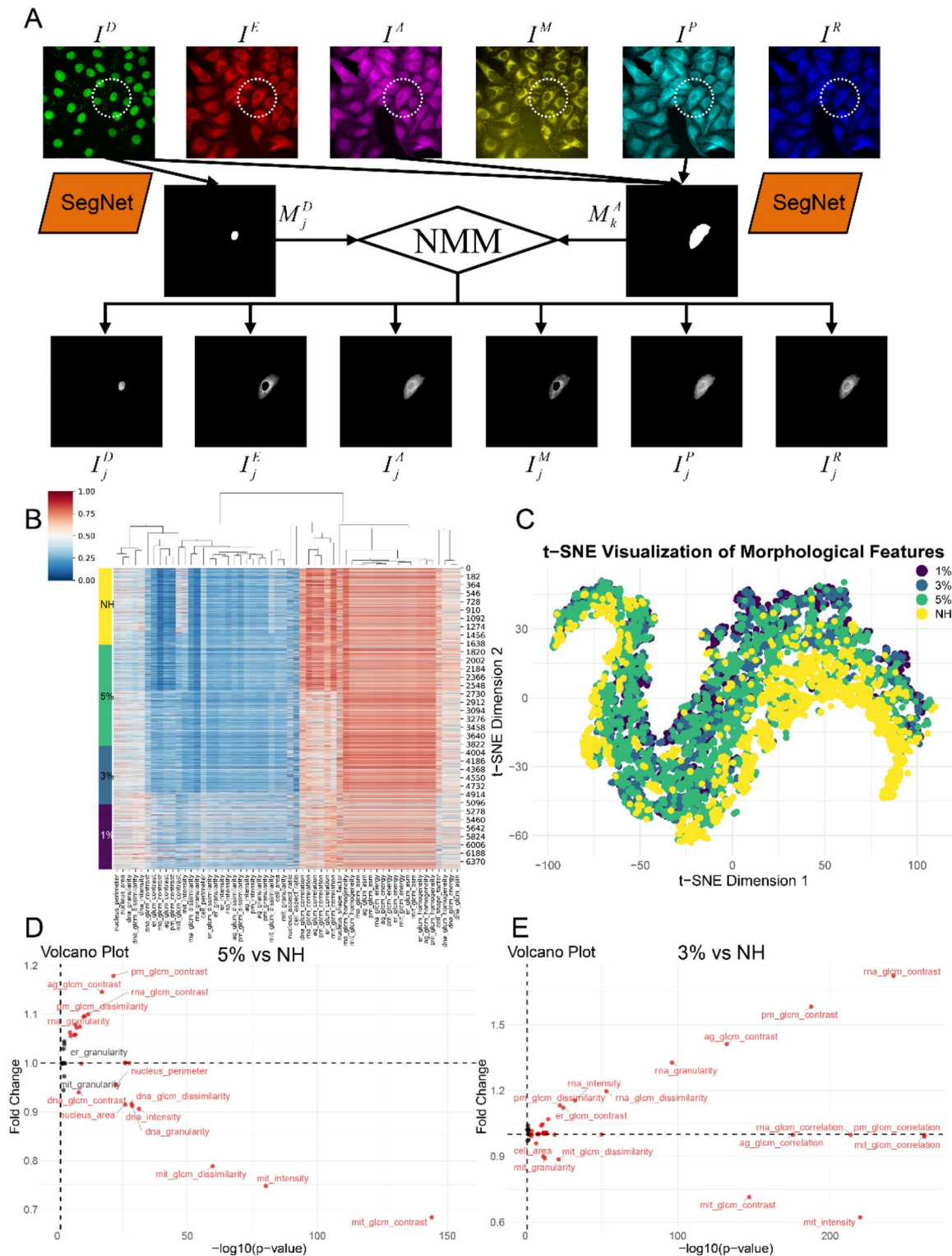


**Fig. 3** Extraction and measurement of subcellular structures. **A**. Overview of the process for extracting 6 types of subcellular structures. **B**. A heatmap of 56 morphological features for 6535 cells exposed to varying levels of oxygen concentration. The heatmap displays the normalized values of cell morphological features. The groups to which the cells belong are annotated in the bar on the left side of the figure. Results of feature clustering are marked at the top of the figure. **C**. T-SNE visualization of the distribution of cell morphological feature space. The morphological feature data of all cells are reduced to two-dimensional space and displayed in a coordinate system, with cells from different groups represented in different colors. **D**, **E**. Volcano plots showing the differences in morphological features between the 5%  $O_2$  group vs. NH group, and the 3%  $O_2$  group vs. NH group, respectively. Red indicates features with significant differences. NH indicates normoxia group

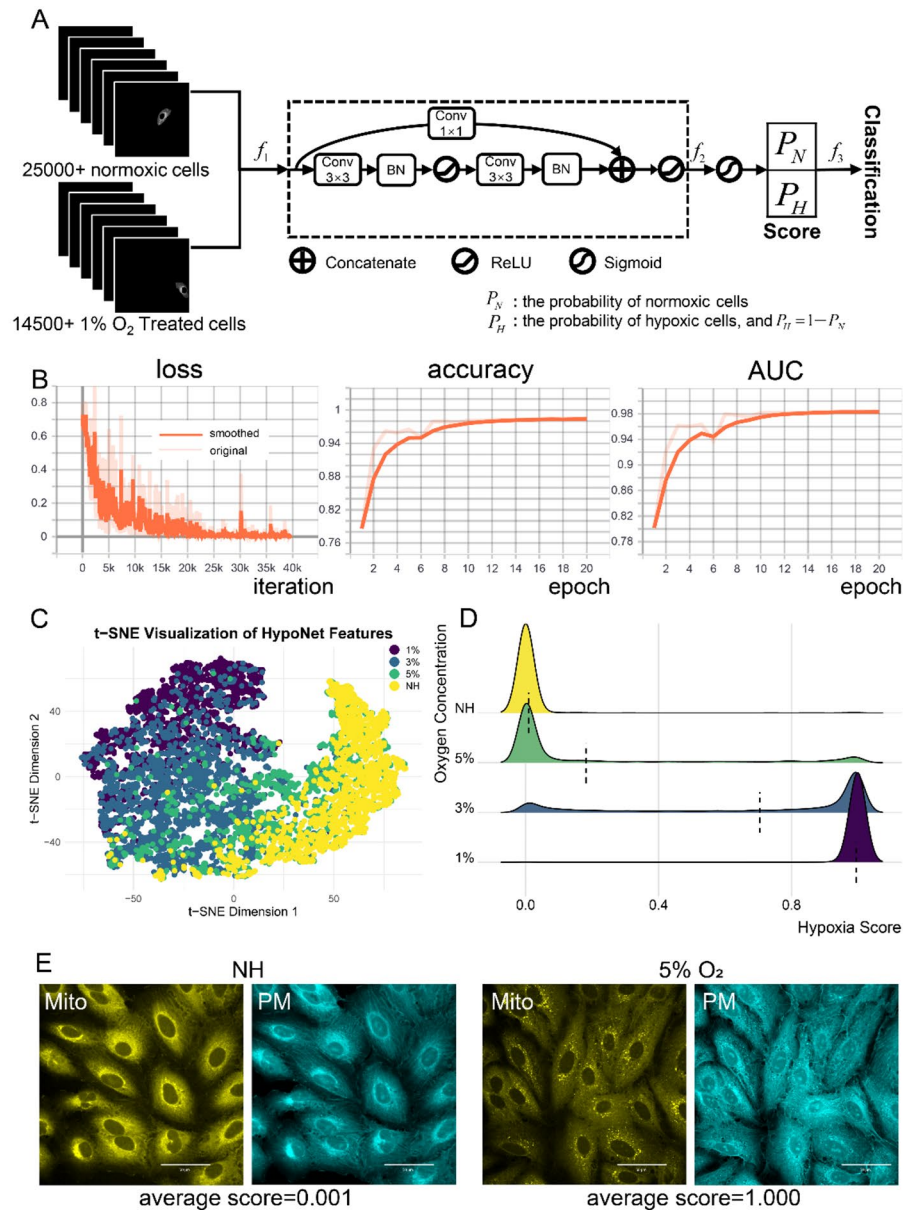


**Fig. 4** Construction of deep-learning based HypoNet. **A**. Design and training framework of HypoNet. The input data is six-channel single-cell images. The dashed box contains a representative residual block structure of ResNet-50, of which there are 16 in the network.  $f_1$  represents Eq. 3, along with a  $7 \times 7$  convolutional layer and pooling layer.  $f_2$  denotes the top pooling layer and the fully connected layers.  $f_3$  signifies the argmax function. **B**. Training loss, validation accuracy and AUC of HypoNet, where the light color represents the original curve, and the dark color represents the curve after smoothing. **C**. Visualization using t-SNE of the weights of the top convolutional layer of HypoNet flattened after inferring on A549s treated with four different hypoxia stress levels. **D**. Hypoxia score distribution calculated by HypoNet for A549s treated with four different hypoxia stress levels. Dashed lines represent the average hypoxia score of different oxygen concentration groups. **E**. Cell Painting images depicting morphological alterations in A549s under normal and 5%  $O_2$  hypoxic conditions, as identified using HypoNet. The average scores are calculated by taking the mean of all cell scores determined by HypoNet within full-field image

#### Exploring drug efficacy against HAPE via HypoNet

To further validate the practicality of HypoNet, we meticulously selected 11 agents with potential anti-hypoxic effects at the cellular level for drug screening. These agents included tetramethylpyrazine (TMP),

tanshinone IIA (TS IIA), salvianolic acid B (SAL B), salvianolic acid C (SAL C), 20(S)-ginsenoside Rh2 (RH2), acetazolamide (ACE), catechin, resveratrol (RES), ferulic acid (FA), compound Danshen dripping pills (DSDW), and Hongyi capsules (HYJN). Although previous reports

**Table 1** Performance comparison of HypoNet against other neural network architectures on two independent test sets

Sets	Model	Accuracy (%)	Recall (%)	Precision (%)	F1-score (%)	AUC
A549	HypoNet	<b>84.7</b>	<b>81.9</b>	96.7	<b>88.7</b>	<b>0.808</b>
	VGG-16	78.7	75.0	<b>98.7</b>	85.2	0.723
	GoogleNet	82.6	79.2	97.5	87.4	0.778
	Xception	78.7	76.0	95.9	84.8	0.731
	Deep-SeSMo	71.4	72.4	87.3	79.1	0.663
HPMEC	HypoNet	<b>88.9</b>	<b>87.4</b>	96.7	<b>91.8</b>	<b>0.856</b>
	VGG-16	75.9	73.4	98.2	84.0	0.667
	GoogleNet	81.9	78.7	<b>98.6</b>	87.5	0.750
	Xception	79.6	77.2	97.1	86.0	0.723
	Deep-SeSMo	42.9	67.3	22.4	33.7	0.513

indicate potential anti-hypoxic or anti-altitude sickness effects of these agents, their role in mitigating HAPE, especially regarding the permeability of the alveolar-capillary barrier during the cellular hypoxic response in the lungs, remains to be explored [1]. Considering the extremity of hypoxic conditions used in the pre-trained model, we chose 5% O<sub>2</sub> as the stress condition for drug screening to ensure the reversibility of cellular hypoxic responses and comparability of hypoxia fractions. By comparing the average hypoxia scores of the NH group, NH group, and 11 different hypoxia treatment groups, we screened for agents that protected against morphological alterations induced by hypoxia. Through multiple rounds of dosing and Cell Painting, we collected more than 15,000 full-field images of A549s and 18,000 full-field images of HPMECs. Using SegNet and NMM, we successfully extracted over 160,000 subcellular structure images of A549s and 180,000 subcellular structure images of HPMECs. All these images had a resolution of 1080 × 1080 and were not used in training previously.

After preprocessing, these subcellular structure images were fed into HypoNet for hypoxia scoring, and we subsequently computed the average hypoxia score for all cells in each respective group (Fig. 5A, B). The results indicated that the hypoxic response in A549s was alleviated after treatment with FA, RES, SAL C, and DSDW compared to the HY group. In contrast to A549s, HPMECs were more sensitive to the drugs, with all agents except Acetazol showing some degree of anti-hypoxic effect, possibly due to their nature as normal rather than tumor cells. We selected agents effective for both cell types, including FA, RES, SAL C, and DSDW, as candidate anti-HAPE agents.

#### Ex vivo effects of the candidates in 3D-alveolus chip models

To validate the reliability of our proposed drug screening method, we used OoC technology to compare the effects of top and bottom drugs identified through screening. We focused on three monomers effective for both cell types (FA, RES, and SAL C) and drug ineffective for both

cell types (ACE) for validation, based on the hypoxia scores. In order to simulate the human alveolar-capillary barrier, we cultivated A549s and HPMECs on opposite sides of the chip to represent the lung epithelium and microvasculature, together constituting an alveolus chip. The integrity of this barrier was successfully detected using immunofluorescence staining for cadherins and tight junction proteins (Fig. 5C). On this basis, we performed three-dimensional reconstruction of the confocal images on the chip, providing a more intuitive observation of cell growth and adhesion (Fig. 5D). The images from different perspectives clearly demonstrated our successful replication of the human alveolar-capillary barrier (Fig. 5E, F).

To assess the protective effects of FA, RES, SAL C and ACE on the alveolar-capillary barrier, we analyzed the permeability of lung chips post-treatment. Our findings revealed that hypoxia alone could lead to increased permeability of the alveolar-capillary barrier, even without a mechanical cause [4]. Furthermore, FA, RES, and SAL C significantly reduced permeability compared to the HY and ACE groups (Fig. 5G, S9), suggesting that these compounds were effective in mitigating damage to the alveolar-capillary barrier caused by hypoxia, and validating the predictive capability of HypoNet for this effect. Further, we attempted to investigate how these drugs influenced the permeability of the air-blood barrier. We selected VEGF, a key modulator of alveolar-capillary barrier permeability particularly in lung injury scenarios as a target to explore the mechanisms by which these three molecules protected the air-blood barrier permeability [29]. The cytokine analysis results indicated that within our alveolus chips, FA, RES, and SAL C markedly decreased the expression of VEGF in A549 and HPMECs when exposed to hypoxic conditions, while ACE was somewhat less effective (Fig. 5H, I). These results highlighted the significant role that FA, RES, and SAL C played in influencing key regulators that maintained the integrity of the alveolar-capillary barrier such as VEGF during hypoxic conditions, thereby offering a protective strategy against HAPE.

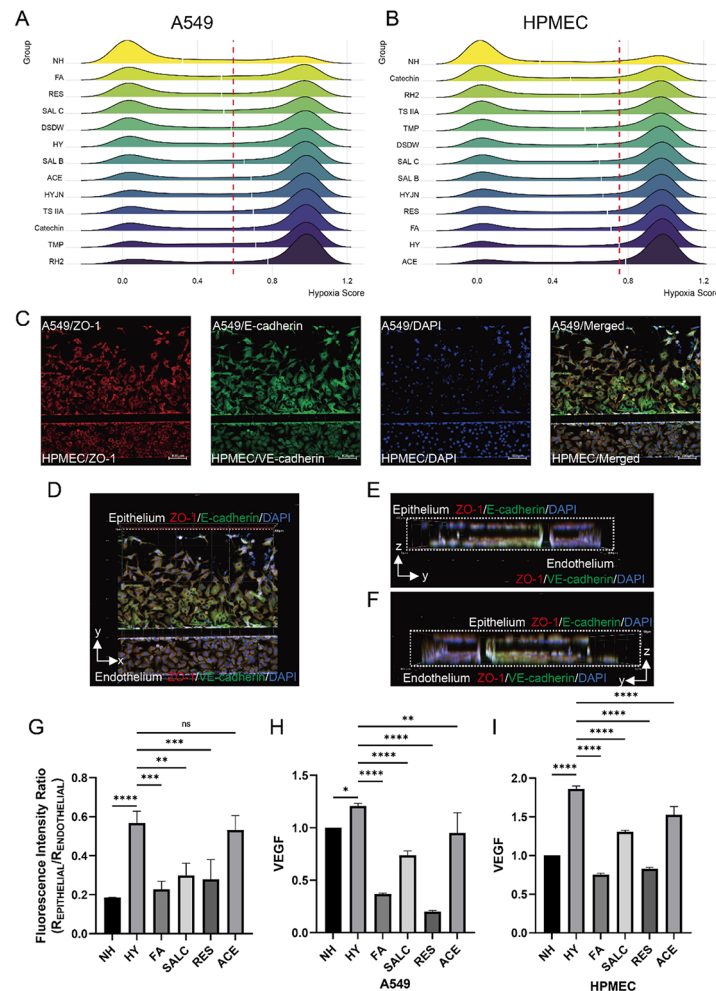


**Fig. 5** HypoNet-based drug screening and alveolus chip validation. **A, B.** Hypoxia score distribution calculated by HypoNet for A549s and HPMECs under various agent interventions. Except for the NH group, all other groups were cultured in a 5%  $O_2$  environment. White solid lines represent the average hypoxia score for different groups, while the red dashed line represents the average hypoxia score for the 5%  $O_2$  (HY) group, which is used as a threshold for drug screening. **C.** Immunofluorescent staining of A549 and HPMECs co-cultured on an OoC under normal oxygen level, displaying channels for Zonula Occludens-1 (ZO-1), Epithelial Cadherin (E-cadherin), Vascular Endothelial-cadherin (VE-cadherin), and DAPI, along with a merged image. **D-F.** 3D reconstructed confocal images shown from different angles of the alveolus chip, illustrating the adhesion and growth of alveolar epithelium (A549) and pulmonary microvascular endothelium (HPMEC) cells. **G.** The effect of different treatments on the ratio of average fluorescence intensity between endothelial and epithelial cells ( $n = 3$ ). The data in each bar indicate the ratio of Relative Fluorescence Units (R). This ratio is derived from measuring the fluorescence of FITC-dextran as it diffuses into the epithelial channel, from the endothelial channel. **H, I.** Expression of VEGF measured by ELISA in A549s and HPMECs within the alveolus chip under a 5%  $O_2$  environment (HY) and treated with FA, SA L C, RES and ACE ( $n = 3$ ). Values are expressed as fold changes relative to the NH group (mean  $\pm$  SD). The data were analyzed by one-way ANOVA. \*\*\*\* $p < 0.0001$ , \*\*\* $p < 0.001$ , \*\* $p < 0.01$ , \* $p < 0.05$  vs. HY group; ns no significance

### FA and RES generated good protective effects against LPS-induced HAPE in mouse model

Next, we evaluated the protective effects of FA and RES in vivo using an LPS-induced HAPE mouse model. As shown in Figs. 6A and 66% of mice treated with LPS and living in a hypoxic chamber (HY group) died within 24 h. In comparison, the survival rates were significantly increased to 100% after FA treatment, as in the NH group. Also, RES increased the survival rate to 67%. Besides, a notable decrease in body weight was observed in HY. FA and RES treatment considerably alleviated the body weight loss induced by LPS and hypoxia exposure

(Fig. 6B). To further evaluate the effect of FA and RES on pulmonary permeability, the absorbance of Evan's Blue dye in lung tissues was measured. Significant increases in pulmonary permeability, as indicated by higher  $OD_{620}$  values, were detected in HY mice. In contrast, FA and RES treatments reduced pulmonary permeability to the level close to that of the NH group (Fig. 6C, D). Moreover, FA and RES treatments markedly reduced the concentrations of proinflammatory cytokines (VEGF, IL-6, and TNF- $\alpha$ ) in the BALF of mice in the NH group, highlighting their anti-inflammatory effects (Fig. 6E-G). Additionally, Western blot analysis was performed to detect

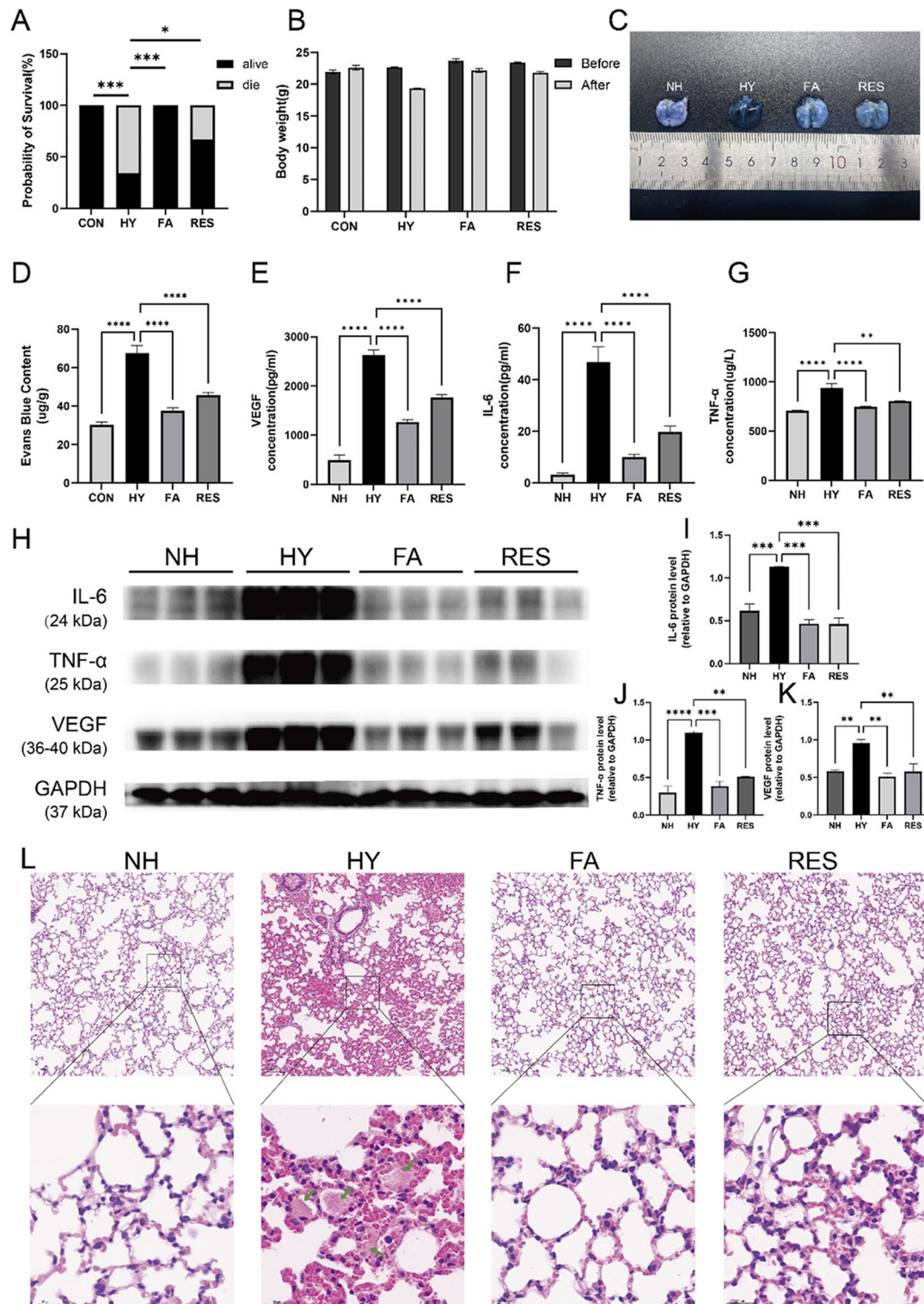


**Fig. 6** (See legend on next page.)

cytokine expressions and alveolar capillary permeability in lung tissues, and found that FA and RES treatments resulted in a notable reduction in the levels of IL-6, TNF- $\alpha$ , and VEGF (Fig. 6H-K, S10, S11). Finally, histological

analysis using H&E staining revealed that the pulmonary tissue of the HY group exhibited destroyed alveolar structure, thickened alveolar walls, and extravasated fluid into alveolar cavity (Fig. 6L). In contrast, FA and

(See figure on previous page.)

**Fig. 6** FA and RES effectively alleviated LPS-induced HAPE in vivo. **A.** Survival rates of mice treated with NH ( $n=12$ ), HY ( $n=12$ ), FA ( $n=12$ ), and RES ( $n=12$ ),  $*p<0.05$  and  $***p<0.001$ , by two-tailed Chi-square test. **B.** Changes in body weight (mean  $\pm$  SD) of mice treated with NH ( $n=12$ ), HY ( $n=4$ ), FA ( $n=12$ ), and RES ( $n=8$ ) before and after the experiment. **C, D.** 2% Evan's Blue dye was administered via tail vein injection. One hour later, lung homogenates were incubated with formamide, centrifuged, and the supernatant's absorbance at 620 nm was measured to determine tissue permeability, presented as OD<sub>620</sub> per gram of dry weight,  $****p<0.0001$  by one-way ANOVA. **E, F, G.** Mice ( $n=6$  per group) were euthanized after hypoxia exposure, and the concentrations of VEGF, IL-6, and TNF- $\alpha$  in the BALF were measured using ELISA kits (mean  $\pm$  SD),  $**p<0.01$  and  $****p<0.0001$  by one-way ANOVA. **H-K.** Lung proteins were analyzed by Western blot to detect markers of inflammation and alveolar capillary permeability using corresponding antibodies ( $n=3$  per group). GAPDH was used as an internal control,  $**p<0.01$ ,  $***p<0.001$  and  $****p<0.0001$  by one-way ANOVA. Molecular weight markers are shown on the right. Data were obtained from two independent experiments. L. Mice ( $n=4$  per group) were euthanized after hypoxia exposure, and lung tissues were collected for analysis. Representative images of histological analyses of lung tissues by H&E staining (scale bar = 100  $\mu$ m). Magnified views of the boxed regions for each image are shown below (scale bar = 20  $\mu$ m). Green arrows indicate pink patches suggesting inflammation and extravasation of fluid into lung tissue

RES treatments mitigated these changes, preserving lung tissue architecture and reducing inflammation. These results collectively demonstrated that FA and RES effectively protected against LPS-induced HAPE by preserving pulmonary permeability, reducing inflammation, and maintaining alveolar-capillary barrier integrity.

## Discussion

Given the complexity of HAPE's mechanisms and the ambiguity surrounding therapeutic targets, phenotypic drug screening has emerged as a promising strategy for discovering anti-HAPE drugs. Despite the availability of advanced technologies like Cell Painting, deep learning, and OoC, each holding potential for advancing this field, effective strategies for their integrated utilization in drug screening remain limited. In this study, we established a deep learning-driven pipeline (CPHNet) for screening anti-HAPE agents based on morphological alterations identified through Cell Painting, which introduced the 3D-alveolus chip and animal models as validation tools for screening results.

Initially, we developed SegNet for the dual segmentation of nucleus and membrane structures from multi-channel full-field cell images. CellProfiler (CP) is a software widely used for downstream analysis of Cell Painting images. It employs threshold segmentation to distinguish objects (cells) from the background by defining a pixel intensity threshold. Pixels with intensities above the threshold are considered part of the object (cell), while those below are treated as the background. Adjusting the threshold size can control the outcome of cell segmentation. However, this process requires substantial expertise and experimentation and may not always achieve the desired results. In contrast, our deep-learning-based SegNet requires no manual intervention. This model is capable of rapidly and accurately segmenting cells based on the morphological information in full-field images, while automatically filtering out noise. The evident superiority of our deep-learning-based model over CP in segmenting cell nuclei and membranes highlights the advantages of AI for computer vision (CV) tasks. Furthermore, the comparison of processing speeds

between AI and other methods is striking. The efficiency of SegNet in analyzing images, compared to CP and manual methods, is indicative of the capability of AI to drastically reduce the time required for biomedical image identification.

Subsequently, we innovatively introduced six-channel Cell Painting images into HypoNet, a refined deep neural network designed for end-to-end feature assessment and phenotypic classification. The novelty of this idea is its ability to comprehensively uncover diverse substructural changes in cells, mitigating potential interference arising from their coexistence in the same channel. When compared with other neural network architectures, we observed that while shallow neural networks like DeepSeSMo are effective in low-resolution single-cell image recognition [17], deeper neural networks are more adept at avoiding underfitting, especially with sufficient high-content cell images derived from Cell Painting techniques (Fig. S6). However, this binary framework presents limitations, particularly in failing to capture the varying degrees of cellular hypoxia induction, a detail that could be paramount in contexts like drug screening. Intriguingly, we observed that while responses at the individual cell level may seem binary, an analysis at the population level unveils a more subtle and gradated response that correlates with the intensity of hypoxic stress. Additionally, the distinctive distribution patterns in the top layer parameters of HypoNet suggest that our model is adept at detecting subtle variations in cellular responses to different levels of hypoxic stress. This underscores the superiority of deep learning over traditional image analysis techniques in decoding complex biological phenomena, confirming our hypothesis. Furthermore, the hypoxia scoring method based on HypoNet provides a quantitative tool for assessing the extent of hypoxia in cells, offering invaluable insights for research fields such as drug screening, where a comprehensive understanding of cellular responses to hypoxia is essential.

Finally, we applied our proposed CPHNet to evaluate 11 agents, successfully identifying FA, RES, and SAL C with potential effectiveness against HAPE. These three drugs have been previously reported to have anti-hypoxia

effects [30–32]. However, reports on the effectiveness of these three drugs in protecting against HAPE are limited. This study reveals that FA and RES exhibit potent protective activity both *ex vivo* and *in vivo*. Specifically, in the 3D-alveolus chip model (*ex vivo*), both FA and RES significantly preserved the integrity of the alveolar-capillary barrier under hypoxic conditions. In the mouse model (*in vivo*), these agents not only improved survival rates but also reduced pulmonary edema and inflammation, as indicated by decreased levels of pro-inflammatory cytokines and reduced pulmonary permeability. Our findings highlight the potential of FA and RES as therapeutic agents for HAPE, emphasizing the importance of further clinical investigations to fully understand their protective mechanisms and optimize their usage in high-altitude medicine.

These results demonstrate that deep neural networks (DNNs) can significantly simplify the Cell Painting analysis workflow. By leveraging these advanced methods, it's possible to quickly and accurately extract phenotypic information from cell images, far surpassing the capabilities of traditional threshold segmentation methods like CP. The utilization of DNNs significantly surpasses simple machine learning methods in both enhancing the precision of feature extraction and deepening the understanding of variations in cellular morphology. In fact, this new paradigm of drug discovery can be extended to other complex diseases, as long as suitable *in vitro* and *in vivo* models can be identified.

While our study illustrates the potential of an AI-driven approach to identify anti-HAPE agents, several inherent limitations must be acknowledged. First, the effectiveness of the identified agents was evaluated primarily under controlled laboratory conditions, which may not fully capture the complex physiological environment encountered at high altitudes. Second, our deep learning models rely heavily on the quality and diversity of the training data, and their ability to generalize to untested conditions or different cell types remains to be thoroughly evaluated. Moreover, although A549 cells are widely used in pulmonary research for their capacity to mimic certain aspects of alveolar epithelial function, they are derived from a lung adenocarcinoma and may exhibit altered responses to hypoxia compared with primary alveolar epithelial cells. This factor could potentially influence the morphological features observed in our study. To advance toward clinical application, several steps are necessary. Collaboration with clinicians and researchers in mountain medicine will be crucial for translating these findings into preventive strategies or treatments for individuals at risk of HAPE. Additionally, expanding our AI model dataset to include a wider range of cell types and hypoxic conditions could improve model robustness and applicability to various altitude-related health issues. Finally, future

studies should consider using primary alveolar epithelial cells or other non-cancerous cell lines to validate our findings and ensure broader generalizability.

## Conclusions

In summary, we developed and trained a deep learning-based drug screening pipeline, CPHNet, to automatically detect morphological changes in Cell Painting images, potentially aiding in the identification of agents for HAPE intervention. Although this study marks an important step in applying phenotypic drug discovery approaches to HAPE, it should be viewed as part of an ongoing process rather than a definitive solution. By integrating advanced deep learning models with Cell Painting and OoC methods, our work offers tools to address challenges traditionally faced by pharmacologists, such as improving both the precision and efficiency of drug screening and further elucidating mechanisms of drug action. Consequently, this study contributes to the evolving field of drug discovery while suggesting new avenues for tackling complex pharmacological questions.

## Abbreviations

AI	Artificial intelligence
AUC	Area under the curve
DMEM	Dulbecco's modified Eagle medium
DNN	Deep neural network
FA	Ferulic acid
FBS	Fetal bovine serum
H&E	Hematoxylin and eosin
HBSS	Hank's balanced salt solution
HAPE	High altitude pulmonary edema
HCS	High content screening
HPMEC	Human pulmonary microvascular endothelial cell
IoU	Intersection over union
mAP	Mean average precision
MoA	Mechanism of action
OoC	Organ-on-a-chip
PFA	Paraformaldehyde
RES	Resveratrol
RGB	Red green blue
t-SNE	t-distributed stochastic neighbor embedding

## Supplementary Information

The online version contains supplementary material available at <https://doi.org/10.1186/s12931-025-03173-1>.

Supplementary Material 1

Supplementary Material 2

## Acknowledgements

We would like to thank Xian-sheng Lu for his contributions to improving the language of the manuscript.

## Author contributions

W.Z., D.S., and Y.G. conceived the research study. X.Y., C.H., and Z.B. conducted the Cell Painting experiments, collected the images, and performed the image preprocessing. D.S., X.Y., and X.T. labeled the Cell Painting images for the segmentation task. D.S., P.S., and Y.H. developed and evaluated the deep learning models used in the study. X.Y., C.H., and C.J.H.F. conducted the alveolus chip experiments. X.Y., Z.N., and N.W. carried out the animal

experiments. D.S., X.Y., W.Z., and Y.L. wrote the manuscript. All authors reviewed and approved the manuscript.

#### Funding

This study was supported by grants from National Natural Science Foundation of China (Grant No. 82405196) and the Innovation Team and Talents Cultivation Program of the National Administration of Traditional Chinese Medicine (Grant No. ZYYCXTD-D-202207).

#### Data availability

Custom code for DNN training, validation, and hypoxia scoring based on CPHNet is available at GitHub repository [<https://github.com/sundezhi3799/CPHNet>]. Data will be made available on request.

#### Declarations

##### Ethics approval and consent to participate

The animal experiments were conducted in accordance with national and institutional guidelines, and the experimental protocols were approved by the Ethics Committee of Animal Experiments at the Beijing Institute of Radiation Medicine (Approval number: IACUC-DWZX-2022-602).

##### Consent for publication

Not applicable.

##### Competing interests

The authors declare no competing interests.

Received: 5 September 2024 / Accepted: 28 February 2025

Published online: 08 March 2025

#### References

- Bärtsch P, Swenson ER. Clinical practice: acute high-altitude illnesses. *N Engl J Med*. 2013;368(24):2294–302.
- Woods P, Alcock J. High-altitude pulmonary edema. *Evol Med Public Health*. 2021;9(1):118–9.
- Maggiorini M. High altitude-induced pulmonary oedema. *Cardiovasc Res*. 2006;72(1):41–50.
- Swenson ER, Bärtsch P. High-altitude pulmonary edema. *Compr Physiol*. 2012;2(4):2753–73.
- El Alam S, Pena E, Aguilera D, Siques P, Brito J. Inflammation in pulmonary hypertension and edema induced by hypobaric hypoxia exposure. *Int J Mol Sci*. 2022;23(20):12656.
- Zhou W, Liu K, Zeng L, He J, Gao X, Gu X, et al. Targeting VEGF-A/VEGFR2 Y949 Signaling-Mediated vascular permeability alleviates hypoxic pulmonary hypertension. *Circulation*. 2022;146(24):1855–81.
- Corti F, Ristori E, Rivera-Molina F, Toomre D, Zhang J, Mihailovic J, et al. Syndecan-2 selectively regulates VEGF-induced vascular permeability. *Nat Cardiovasc Res*. 2022;1(5):518–28.
- Dai Z, Zhu MM, Peng Y, Jin H, Machireddy N, Qian Z, et al. Endothelial and smooth muscle cell interaction via FoxM1 signaling mediates vascular remodeling and pulmonary hypertension. *Am J Respir Crit Care Med*. 2018;198(6):788–802.
- Wang Y, Li X, Niu W, Chen J, Zhang B, Zhang X, et al. The alveolar epithelial cells are involved in pulmonary vascular remodeling and constriction of hypoxic pulmonary hypertension. *Respir Res*. 2021;22(1):134.
- Bray MA, Singh S, Han H, Davis CT, Borgeson B, Hartland C, et al. Cell painting, a high-content image-based assay for morphological profiling using multiplexed fluorescent dyes. *Nat Protoc*. 2016;11(9):1757–74.
- Moshkov N, Becker T, Yang K, Horvath P, Dancik V, Wagner BK, et al. Predicting compound activity from phenotypic profiles and chemical structures. *Nat Commun*. 2023;14(1):1967.
- Rohban MH, Singh S, Wu X, Berthet JB, Bray MA, Shrestha Y, et al. Systematic morphological profiling of human gene and allele function via cell painting. *Elife*. 2017;6:e24060.
- Akbarzadeh M, Deipenwisch I, Schoelermann B, Pahl A, Sievers S, Ziegler S, et al. Morphological profiling by means of the cell painting assay enables identification of tubulin-targeting compounds. *Cell Chem Biol*. 2022;29(6):1053–e643.
- Pratapa A, Doron M, Caicedo JC. Image-based cell phenotyping with deep learning. *Curr Opin Chem Biol*. 2021;65:9–17.
- Ma S, Wu J, Liu Z, He R, Wang Y, Liu L, et al. Quantitative characterization of cell physiological state based on dynamical cell mechanics for drug efficacy indication. *J Pharm Anal*. 2023;13(4):388–402.
- Malandraki-Miller S, Riley PR. Use of artificial intelligence to enhance phenotypic drug discovery. *Drug Discov Today*. 2021;26(4):887–901.
- Kusumoto D, Seki T, Sawada H, Kunitomi A, Katsuki T, Kimura M, et al. Anti-senescent drug screening by deep learning-based morphology senescence scoring. *Nat Commun*. 2021;12(1):257.
- Wang CY, Bochkovskiy A, Liao HYM, editors. YOLOv7: Trainable bag-of-freebies sets new state-of-the-art for real-time object detectors. *Proceedings of the IEEE/CVF Conference on Computer Vision and Pattern Recognition*; 2023.
- McGibbon M, Money-Kyrle S, Blay V, Houston DR. SCORCH: improving structure-based virtual screening with machine learning classifiers, data augmentation, and uncertainty Estimation. *J Adv Res*. 2023;46:135–47.
- Chen X, Xun D, Zheng R, Zhao L, Lu Y, Huang J, et al. Deep-Learning-Assisted assessment of DNA damage based on foci images and its application in High-Content screening of lead compounds. *Anal Chem*. 2020;92(20):14267–77.
- Schorpp K, Bessadok A, Biibosunov A, Rothenaigner I, Strasser S, Peng T, et al. CellDeathPred: a deep learning framework for ferroptosis and apoptosis prediction based on cell painting. *Cell Death Discov*. 2023;9(1):277.
- Bhattachar S, Sikri G, Thapa B. Altitude-induced pulmonary hypertension on one-day rapid ascent of Mount Fuji: incidence and therapeutic effects of sildenafil. *Echocardiography*. 2016;33(9):1441.
- Service RF, Bioengineering. Lung-on-a-chip breathes new life into drug discovery. *Science*. 2012;338(6108):731.
- Zhou X, Jiang Y, Wang Y, Fan L, Zhu Y, Chen Y, et al. Endothelial FIS1 desumoylation protects against hypoxic pulmonary hypertension. *Circ Res*. 2023;133(6):508–31.
- Chai S, Wang W, Liu J, Guo H, Zhang Z, Wang C, et al. Leptin knockout attenuates hypoxia-induced pulmonary arterial hypertension by inhibiting proliferation of pulmonary arterial smooth muscle cells. *Transl Res*. 2015;166(6):772–82.
- Bueno-Beti C, Hadri L, Hajjar RJ, Sassi Y. The Sugen 5416/hypoxia mouse model of pulmonary arterial hypertension. *Methods Mol Biol*. 2018;1816:243–52.
- Zhang M, Wang P, Luo R, Wang Y, Li Z, Guo Y, et al. Biomimetic human disease model of SARS-CoV-2-Induced lung injury and immune responses on organ chip system. *Adv Sci (Weinh)*. 2021;8(3):2002928.
- Hu YL, DeLay M, Jahangiri A, Molinaro AM, Rose SD, Carbonell WS, et al. Hypoxia-induced autophagy promotes tumor cell survival and adaptation to antiangiogenic treatment in glioblastoma. *Cancer Res*. 2012;72(7):1773–83.
- Ourradi K, Blythe T, Jarrett C, Barratt SL, Welsh GI, Millar AB. VEGF isoforms have differential effects on permeability of human pulmonary microvascular endothelial cells. *Respir Res*. 2017;18(1):116.
- Luo C, Zhang Y, Guo H, Han X, Ren J, Liu J. Ferulic acid attenuates hypoxia/reoxygenation injury by suppressing mitophagy through the PINK1/Parkin signaling pathway in H9c2 cells. *Front Pharmacol*. 2020;11:103.
- Moreira-Pinto B, Costa L, Felgueira E, Fonseca BM, Rebelo I. Low doses of Resveratrol protect human granulosa cells from Induced-Oxidative stress. *Antioxid (Basel)*. 2021;10(4).
- Shen H, Pei H, Zhai L, Guan Q, Wang G. Salvianolic acid C improves cerebral ischemia reperfusion injury through suppressing microglial cell M1 polarization and promoting cerebral angiogenesis. *Int Immunopharmacol*. 2022;110:109021.

#### Publisher's note

Springer Nature remains neutral with regard to jurisdictional claims in published maps and institutional affiliations.